JQMBiQ‘BM; 7 bi bQH ‘ +?‘QKQbT??2‘B+
J2i2QaT +2 T‘QD2+i

C2 M@J ‘B2 J H?2‘#2- h?B2‘‘v *Q‘# ‘/- : H2 " ‘# ‘v
*H m/2 *QHHBM- . MB2H *‘mbb B‘2- 6HQ‘2M

hQ +Bi2 i?Bb p2‘bBQM,

C2 M@J `B2 J H?2`#2- h?B2``v *Q`# `/- : H2 " `# `v- 6`û/û`B+ JQ` M
BiQ`BM; 7 bi bQH ` +?`QKQbT?2`B+ +iBpBiv, i?2 J2i2QaT +2 T`QD2
8j- TTXRRkd @ RR93X RyXRyydfbRye3e@ykk@yN393@d X ? H@yj3

> G A/, ? H@yj3e3N3y
?iiTb,ff+M‘bX? HXb+B2M+2f? H@yj3e3N3y
am#KBii2/ QM R .2+ kykk

a

a

a

a

a

l

a

a

a

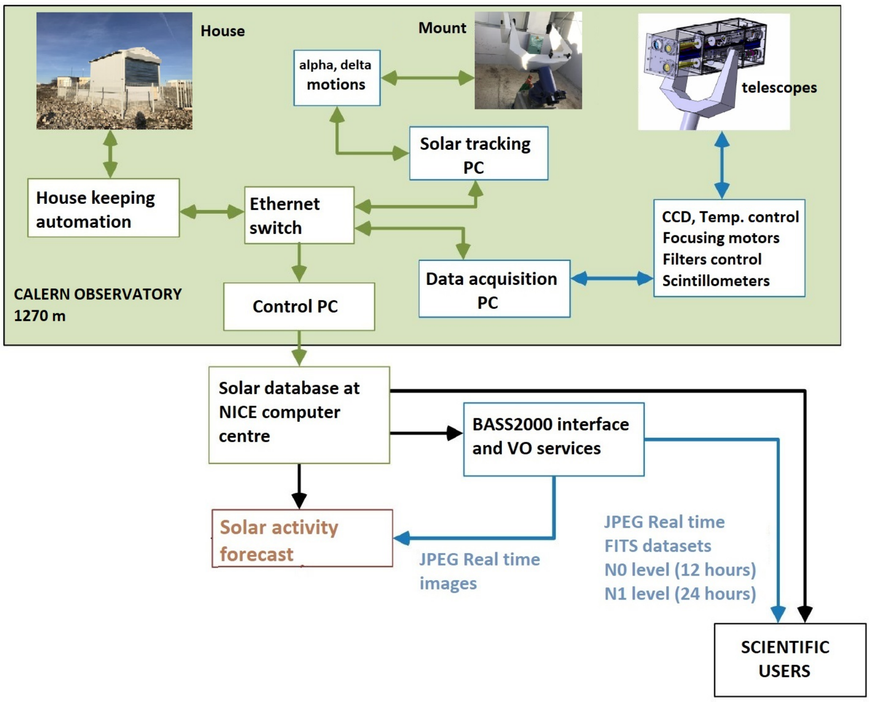
House
Mount
alpha, delta motions
telescopes
Solar tracking PC
House keeping automation
Ethernet switch
CCD, Temp. control
Focusing motors
Filters control
Scintillometers
Data acquisition PC
CALERN OBSERVATORY 1270 m
Control PC
Solar database at NICE computer centre
BASS2000 interface and VO services
Solar activity forecast
JPEG Real time images
JPEG Real time
FITS datasets
N0 level (12 hours)
N1 level (24 hours)
SCIENTIFIC USERS

House and mount at CALERN observatory (1270 m)

a

a

a

a

a

a

a

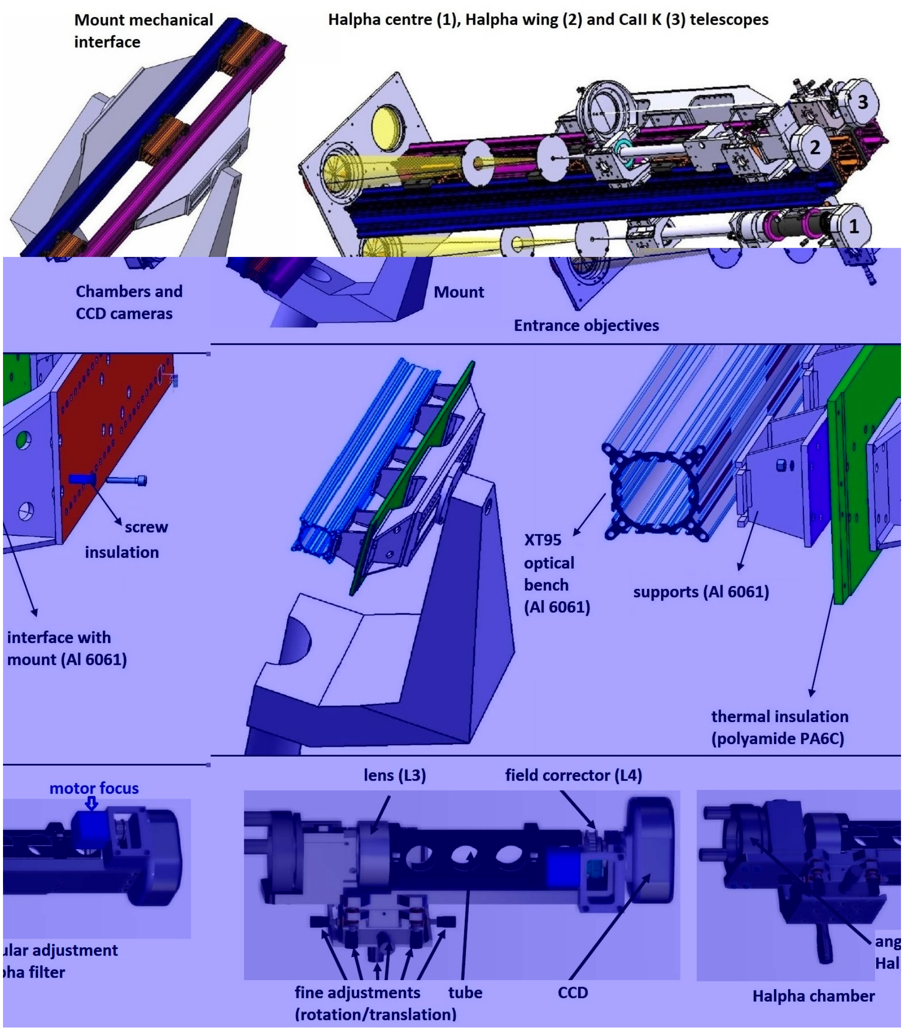

Mount mechanical interface
Halpha centre (1), Halpha wing (2) and CaII K (3) telescopes
3
2
1
Chambers and CCD cameras
Mount
Entrance objectives
screw
insulation
interface with mount (Al 6061)
XT95 optical bench (Al 6061)
supports (Al 6061)
thermal insulation (polyamide PA6C)
motor focus
lens (L3)
field corrector (L4)
fine adjustments (rotation/translation)
tube
CCD
Halpha chamber

a

a

Fig. 4 The theoretical MTF of the Hα (red) and CaII K (blue) telescopes. Abscissa: spatial fequency in km^{-1} or in $arcsec^{-1}$. Cutoff frequencies are indicated (bars). The computed PSFs, in the detector plane, are reported (the pixels correspond to the CCD sampling). The Hα PSF is for the border of the FOV, while the CaII K PSF is for the centre.

Fig. 5 The MTSP Filter bandwidths. Filters have been controlled with the high dispersion spectrograph of Meudon Solar Tower. Left: Hα line without (top) or with (bottom) filter 1. The pupil integrated transmittance (solid line, top) over the surface filter is drawn (0.46 Å FWHM). Middle: Hα line without (top) or with (bottom) filter 2. The pupil transmittance is 0.34 Å FWHM. Right: CaII K line as seen through the two available filters of respectively 1.5 (filter 1, bottom) and 1.4 Å FWHM (spare filter 2, top). The transmittance (solid line) includes K2v, K3 and K2r features, and partially K1v and K1r (v, r letters meaning respectively violet and red wings).

CCD camera (QSI 690, pixel size = 3.69 μm = 0.78 arcsec). The system is protected by an UV/IR cutoff filter. The Airy spot size is 5.9 μm or 1.24 arcsec resolution.

The interference filters were tested with the powerful 14 m spectrograph of Meudon Solar Tower at F/75 (R = 300000, 6 mÅ spectral line sampling in order 15). We found that the central wavelength (CWL) is temperature (T) dependant, according to the law $\Delta\lambda_{CWL} = C\,\Delta T$, where C = 0.07 Å/°C is the measured temperature coefficient. It is also function of the incidence angle θ, and follows the law $\Delta\lambda_{CWL} = K\,\theta^2$ with K =

Fig. 6 The MTSP CaII K channel. Top: the overall design of the telescope. Bottom: details of the chamber. L2/L3 increase the focal length from 820 to 983 mm. Filters are in the image plane at F/12.3. The chamber has a motor focus.

-0.15Å/degree^2. As the theory gives $K = \frac{1}{2}\frac{\lambda_0}{n^2}$ (θ in radians), where n is the effective index of refraction and λ_0 the line wavelength, we derived from the measurements n ≈ 2.0. With an aperture of F/12.3 (half cone of 2.3°), the numeric integration over the light cone shows that the CWL is blue-shifted (-0.41Å), but this is almost compensated (+0.49Å) by the operating temperature (+7°C above the specification of the manufacturer), so that the resulting CWL shift is small in comparison to the FWHM (the transmittance of the filter centre is displayed in Figure 5, right). This figure also reveals that the surface filter is not uniform. We found that that the CWL varies from the centre to the border according to the law $\Delta\lambda_{CWL} = k\, x^2$, where x is the distance to the filter centre. We measured k = -0.006Å/mm^2 and +0.003Å/mm^2 respectively for filters 1 and 2 (the spare filter). It means that the CWL varies between the centre of the solar disk and the limb ($0 \leq x \leq 4.6$ mm), numerically $\Delta\lambda_{CWL}$ = -0.13Å or +0.07Å, respectively for filters 1 and 2. This is less than 10% of the FWHM, so that the effect does not appear obviously in solar images. Figure 7 shows a comparison between the CaII K3 Meudon spectroheliograms (line centre) and MTSP test images (formed at lower altitude due to the larger bandwidth): filaments and prominences are no more visible, but sunspots appear more contrasted; bright faculae look similar, so that the CaII K MTSP channel produces a good magnetic proxy. It is close to the wavelength integration of the spectroheliograph data-cube $I(x,y,\lambda)$ with 0.093 Å resolution) over the MTSP transmittance.

4 The two Hα channels

The two Hα telescopes (Figure 8) have an aperture of 80 mm and 100 mm, respectively for filters 1 and 2. They are composed of a Takahashi TSA102 objective (816 mm focal length) followed by an afocal chamber (magnification 1.2), including a DayStar Quantum Pro Fabry-Pérot filter in the pupil plane. This system introduces field curvature, so that a field corrector (two lenses) forms the final image on an in-

Fig. 7 Comparison of Meudon CaII K3 spectroheliograms and MTSP CaII K images, 26 November 2020. (a) K3 spectroheliogram (30 s surface scan by the slit, square root to decrease the dynamics). (b) the spectroheliograph (x, y, λ) data-cube integrated over the MTSP wavelength transmission curve. (c) the MSTP K image, 1.5 Å FWHM (2 ms exposure time, the waveband covers K2v, K3 and K2r central features of the CaII K line, and partially K1v and K1r wings).

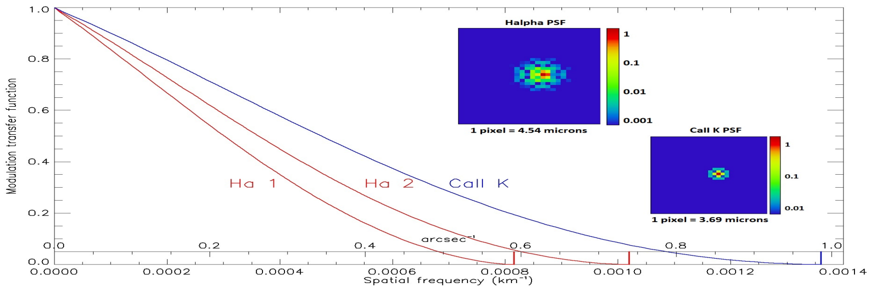

Fig. 8 The MTSP Hα channels. The filter is located in the pupil plane at F/30 inside the L2/L3 afocal system. L4 is a field curvature corrector. The chamber has a motor focus (see also Figure 3). The equivalent focal length is 983 mm, as for CaII K. The beam aperture, in the detector plane, is F/12.3 and F/10.0 respectively for Hα 1 and 2.

terline cooled CCD camera (QSI 660, pixel size = 4.54 µm = 0.96 arcsec). The Airy spot size is 9.8 and 7.9 µm, corresponding to 2.06 and 1.65 arcsec resolution, respectively for telescopes 1 and 2. The system is protected by an UV/IR cutoff filter in full aperture (not drawn). A motor focus is integrated to the chambers.

The calibration of Fabry-Pérot filters has been done with the spectrograph of Meudon Solar Tower, at F/75 (much better than the F/30 filter specification), in order 9 (10 mÅ/pixel). Several tests have been performed for both filters. First of all, we made a scan of the surface in order to produce a pupil cartography of the CWL and FWHM (Figures 9 and 10). For that purpose, the filters (31 mm diameter) were translated (-15 mm ≤ x ≤ 15 mm) in front of the spectrograph slit by Δx = 3 mm steps. I(λ, y) spectral images, with and without filters, were recorded, for various x-positions (top of figures). The wavelength transmittance was derived at several (x, y) locations. The results show that the FWHM of both filters is locally in the range 0.30-0.35 Å, but also that filter 2 is better than filter 1 in terms of CWL uniformity. By integration on the surface, we computed the resulting bandpass for pupil plane application in afocal systems, leading to 0.46 and 0.34 Å, respectively for filters 1 and

Fig. 9 Calibration of Hα filter 1. It was translated by 3 mm steps in the spectrograph focus of the Meudon Solar Tower (F/75). Top: the Hα line through the filter for 9 x-positions of the slit (in mm). The white lines delineate the CWL and FWHM (y-direction). Bottom: the filter cartography. The local FWHM (Å) is displayed at left. CWL fluctuations (Å) are not negligible (at right), so that for pupil plane application, the integrated bandpass is enlarged to 0.46 Å

2. The pupil transmittance is Lorentzian shaped in wavelength and drawn in Figure 5 for both filters.

Fabry-Pérot filters have secondary lobes, cut by a blocking filter. We found, for filter 2, that they appear at ±25 Å from the main lobe with an intensity of only 0.3% (Figure 11). For that filter (0.34 Å FWHM), the measurements provide the value of the finesse (75), the reflection coefficient of the cavity (0.96) and the interference order for Hα line (k = 260).

Meudon spectroheliograph data, which are made of 3D (x, y, λ) data-cubes (0.155 Å wavelength resolution) allow to simulate images using various transmittances. Figure 12 displays Hα images with different filter characteristics, such as a Lorentzian transmittance (0.34 Å FWHM) or a 0.50 Å FWHM five stage Lyot transmittance. It clearly shows that a smaller bandwidth is needed for the Fabry-Pérot to produce contrasts similar to the ones provided by Lyot filters. Indeed, the wavelength curve of Lyot filters drastically cuts the line wings, contrarily to Lorentzian filters which have extended wings. Hence, the photospheric light passes in excess and contaminates the contrast of the chromosphere. When 0.50 Å Lyot filters are sufficient to select the chromosphere, narrower (0.30 Å) Fabry-Pérot devices (such as MTSP filter 2) are required for the same result.

The Solar Tower spectrograph allowed us to explore the angular dependance of MTSP filters and precise the tilt sensitivity (θ) in terms of CWL and FWHM fluctuations. This experience also provided an estimate of the effective index of refraction. For that purpose, the filter was tilted in the range $-3° \le \theta \le +3°$ (Figure 13). The mean CWL variations are fitted by the law $\Delta\lambda_{CWL} = K\,\theta^2$ with K = -0.38 or -0.37

Fig. 10 Calibration of Hα lter 2. Top: the Hα line through the lter for 11 x-positions of the spectrograph slit (in mm). The white lines delineate the CWL and FWHM (y-direction). Bottom: the lter cartography. The local FWHM (Å) is displayed at left. At right, the CWL (Å) uctuations are small, so that the integrated bandpass for pupil plane application (0.34 Å) remains narrow.

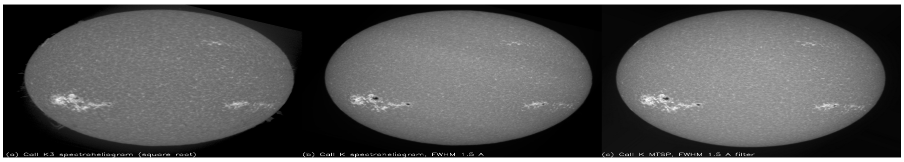

Fig. 11 Secondary transmission peaks of Hα lter 2 in logarithmic intensity scale (wavelength in abscissa).

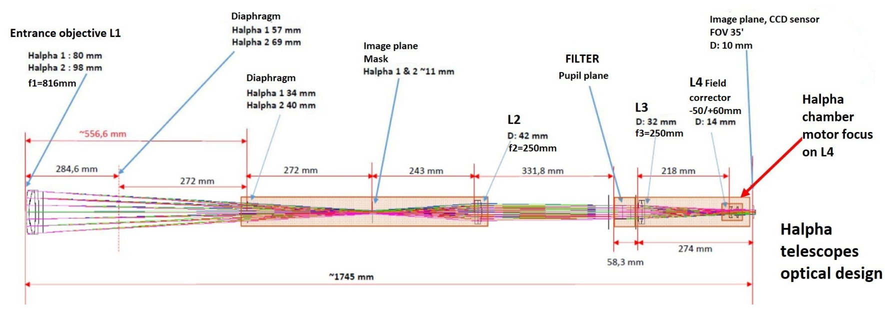

Fig. 12 Simulation of Hα images obtained after ltering the (x, y, λ) spectroheliograph data-cube. (a) Spectroheliogram at line centre, 28 October 2021. (b) Same image, through a 0.34 Å Lorentzian transmission (such as MTSP lter 2). (c) Same image, with a 0.50 Å ve stage Lyot lter, for comparison.

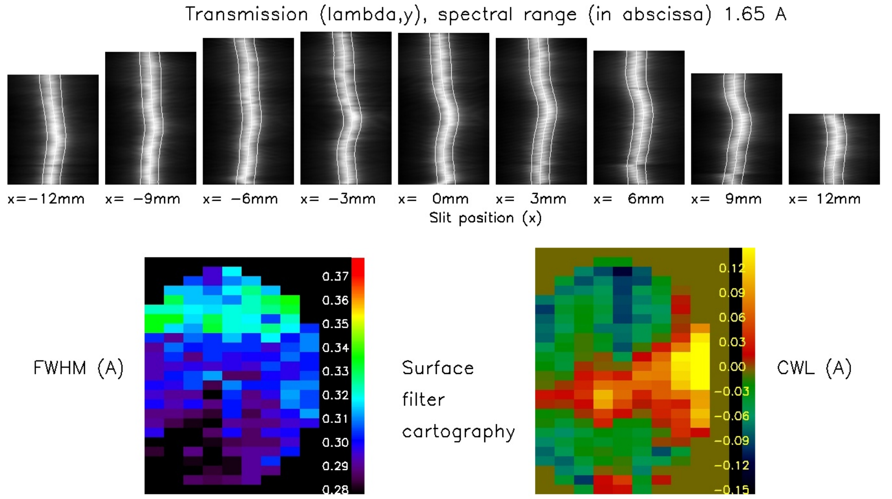

Fig. 13 Effect of the tilt angle on the filter transmission curves (abscissa: wavelength in Å). Tilt values are 0° (in red), ± 0.25°, ± 0.75°, ± 1.25°, ± 1.75°, ± 2.25° and -2.75°. The transmission is blue-shifted with increasing tilt. Thick line: the Hα profile. Dashed line: the envelope of the blocking filter.

Å/degree^2, respectively for filters 1 and 2. For the tilt dependance of the mean bandpass, we found FWHM = 0.33 + 0.064 θ^2 and 0.35 + 0.052 θ^2 (Å), respectively for filters 1 and 2. This means that, for a 1° tilt, the bandpass is locally enlarged to 0.40 Å and blue-shifted of about -0.40 Å. But in the afocal system, at F/30 (half cone angle of 1°), we have to integrate the above formulae over angles, which generates a blue-shift of -0.19 Å (this value was confirmed by the wavelength line scan made with the filter in imagery mode, which produced results of Figure 15). However, the F/30 cone angle is not the only one to consider. The solar diameter is 0.53°, which means that the cone incidence θ varies in the range -0.26° $\leq \theta \leq$ +0.26°. The corresponding blue-shift is, at maximum, -0.024 Å, which can be neglected, so that the CWL should be almost uniform over the solar image.

According to the Fabry-Pérot theory, we have K = - $\frac{1}{2}$ $\frac{\lambda_0}{n^2}$ (where λ_0 is the line wavelength). It allows to derive the effective index of refraction n of the overall filter. We found n $\approx$ 1.62. The distance of secondary lobes is $\frac{2en}{k^2}$ = 25 Å, where k is the interference order (260) and e the thickness of the cavity. Hence, we conclude that e $\approx$ 7.2 mm.

The envelope of transmittance curves of Figure 13 corresponds to the blocking filter. The estimated FWHM is about 4.5 Å; this value, considering a Lorentzian shape, is consistent with the intensity (0.3%) of the secondary peaks of Figure 11.

The CWL depends on the temperature T. We investigated, by the spectroscopic means of the Solar Tower, the effect of temperature changes upon filter 2. The transmittance for temperatures varying from 38 to 48°C is reported in Figure 14. The response is a red-shift corresponding to the linear law $\Delta\lambda_{CWL} = \kappa$ T - 3.84 Å, where T is expressed in °C and κ is the temperature coefficient equal to 0.0874 Å/°C. Hence, it is possible to explore the ± 1.0 Å spectral domain centred on the line, but in

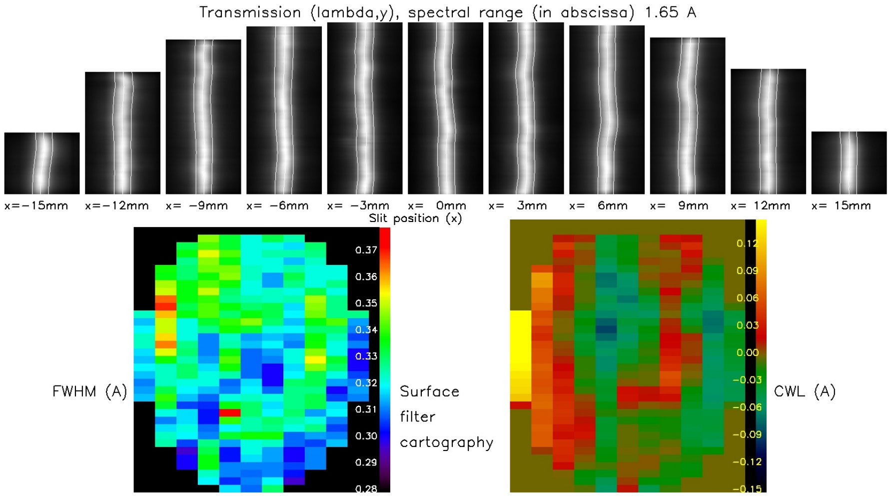

Fig. 14 Effect of the temperature on the filter transmission curves (abscissa: wavelength in Å). Temperature values are 38, 39, 40, 41, 41.8, 42.8, 43.8, 44.7, 45.6, 46.6 and 47.5 C. The transmission is red-shifted with increasing temperature. Thick line: the Hα profile. Dashed line: the envelope of the blocking filter.

practice it is a very slow process. We did not notice any FWHM variation with the temperature.

The last qualification test was performed with the filter alone, in image mode, without any spectrograph. Filter 1 was mounted in the MTSP afocal system, and we explored the wavelength range 6562.0-6563.6 Å by temperature variation. It took a long time, because the filter needs 10 minutes to stabilize at each wavelength increment. We recorded also the fluctuations of the solar flux using a scintillometer, in order to correct intensities measured by the filter due to atmospheric variations. Then, we derived the Hα line profile at the disk centre (Figure 15). We also plotted the line profile got by spectroscopic means, and convolved by the Lorentzian transmittance of the filter, and found both results in good agreement, after correction of the -0.2 Å shift resulting from the F/30 light cone angle.

Finally, Figure 16 presents the typical Hα observations that are scheduled with the above filters. MTSP will provide almost simultaneously two images, the first one in the line wing (filter 1, either the blue or the red wing, but not both), and the second one in the line core (filter 2). We discuss in the next section the application to the detection of fast evolving Doppler-shifted events, such as Moreton waves, which require at least two Hα channels and the high observing cadence of 10-15 s.

5 Moreton waves detection

MTSP is particularly well adapted to the detection of highly dynamic events, such as Moreton waves originating in energetic flares. As the filter performances are comparable to those of the previous Meudon routine (1985-2004), we have chosen two

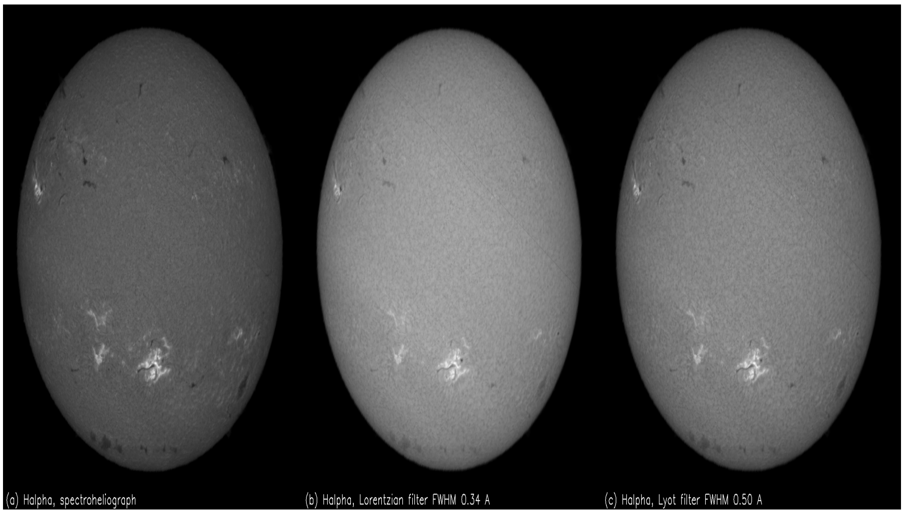

Fig. 15 Hα line profiles got in imagery or spectroscopic mode. Black: MTSP measures resulting from filter temperature variation. Red: the line observed with the large spectrograph of Meudon Solar Tower, and the convolution by the MTSP filter transmittance (dashed). In abscissa: the wavelength (Å) and the corresponding LOS velocity (km s^{-1}).

Fig. 16 Example of MTSP Hα images got during the test campaign of 29 August 2017 with filter 1 (0.46 Å FWHM). (a) MTSP, blue wing. (b) MTSP, line centre (0.34 Å FWHM filter 2 will be used instead in full operation). (c) Meudon spectroheliogram for comparison.

events observed with this instrument in order to anticipate MTSP capabilities. Moreton waves appear in Hα as fronts propagating at typically 500 km s^{-1}. Such velocities in the chromosphere (8000 K) are so highly supersonic ($C_s \approx 10$ km s^{-1}) and superalfvénic ($C_a \approx 10$ km s^{-1} for a 10 G magnetic field) that they are unlikely of chromospheric nature. Such phenomena last only a few minutes and are suspected to be the chromospheric counterpart of coronal waves propagating in the 200 times hotter (1.5 MK) and more tenuous corona under the form of fast magnetosonic shocks ($C_s \approx 150$ km s^{-1}, $C_a \approx 200$ km s^{-1} for a 10 G field). The downward compression of the chromosphere below the front could be the signature of the coronal shock in Hα. Moreton waves occur mainly in X-class flares which are rare events (about one event/year above X5, six events above X10 since year 2000). We have chosen the famous X17.2 flare of 28 October 2003 (Figure 17), after the solar maximum of cycle 23, and the X1.8 event of 14 October 1999, just before the maximum (Figure 18). Largest flares often occur during the descending phase of the solar cycle. In Figure 17 (b,c,d respectively for Hα centre and ± 0.5Å), we have subtracted the reference frame just before the event at the same wavelength. Blue/red colours indicate the sign of the resulting image (blue, or positive, means brighter; red, or negative, means darker). The wave (yellow box) appears as a brightening in Hα core (b). In the red wing subtraction (c), the compression front (R) is negative (or darker) and corresponds to a red-shift. It is followed by the relaxation of the chromosphere (B) appearing positive (or brighter), because blue-shifted. In the blue wing subtraction (d), this is the contrary: R is positive (or brighter), because red-shifted, while B is negative (or darker) with the opposite shift. Figure 15 shows that the order of magnitude of LOS velocities for 0.5 Å shifts is qualitatively 20 km s^{-1}. This example shows that Moreton waves can be detected either by the red or the blue wing. For that reason, MTSP offers only one wing.

Figure 18 presents the X1.8 flare of 14 October 1999, almost 10 times less energetic than the previous one, so that the Moreton event is less contrasted. It shows exactly what will provide MTSP concerning wave detection with one wing. Most events are waited between 2024 and 2028 around the solar maximum (2025) of cycle 25 (but isolated events, as the X1.0 of 28 October 2021, are possible). The Hα centre (a) will be provided by telescope 2, from which a reference frame (just before the event) has been subtracted in (b), showing the brightening front. The Moreton event appears clearly in the red wing with the red-shifted compression front (R) followed by the blue-shifted relaxation front (B). The blue wing could either be chosen. The big difference with the 1985-2004 Meudon routine is the observing cadence (4 times faster) and the spatial resolution (2 times better). Hence, MTSP will provide much more detailed informations to investigate the physics of rare phenomena at the Sun.

6 A possible extension for MTSP

We own a NaD1 5896 Å Fabry-Pérot filter manufactured by DayStar (0.36 Å FWHM), for mounting in an afocal design at F/30 similar to the one of the Hα telescopes described above. Magnetograms of the Sun have been successfully produced in this line (Landé factor 1.33) by Mount Wilson (full disk) or by the Narrow-band Filter Imager (NFI) onboard HINODE for small regions. NaD1 is a Fraunhofer line formed in the low chromosphere above the FeI 6173 Å line observed in the photosphere by the Helioseismic and Magnetic Imager (HMI) onboard SDO. As DayStar filters are linearly polarizing (made of a birefringent material), the incorporation of a Liquid Crystal Variable Retarder (LCVR) at the primary focus, providing $\lambda/4$ fast modulation (Malherbe et al., 2007) suffice to produce alternatively I+V and I-V images (I, V for Stokes parameters). From the circular polarization rate $\frac{V}{I}$ and the weak field theory (see Stenflo (1994)), it is possible to estimate the LOS magnetic field (BLOS) together with the field polarity. Indeed, $\frac{V}{I}$ is proportional to BLOS and $\frac{1}{I}\frac{dI}{d\lambda}$. This quantity depends on the wavelength and is maximum when measured at the inflexion points of the line. Figure 19 displays spectroscopic observations obtained with this

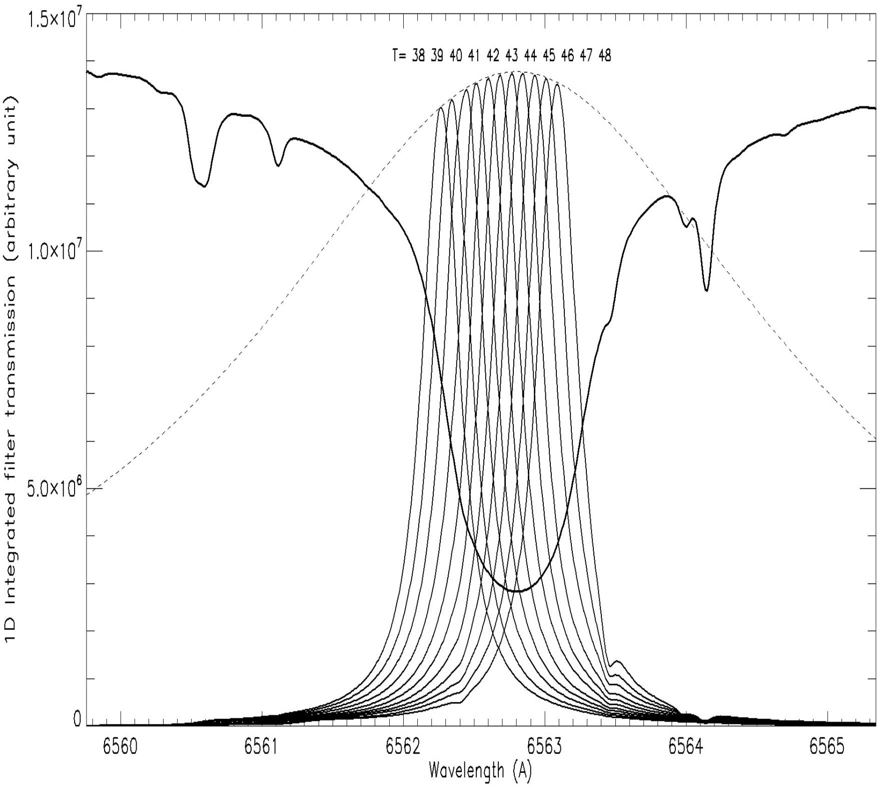

Fig. 17 Moreton event of 28 October 2003 at 11:07 UT. Images, in Hα centre, red and blue wings, were taken with 60 s time step. (a) Hα centre. (b) Hα centre, minus the reference frame at 11:00 UT (event starting time). (c) Hα red wing, minus the reference. (d) Hα blue wing, minus the reference. F, R, B indicate respectively the flare location, red and blue shifts of the compression and relaxation fronts of the Moreton wave (propagation direction = green arrow).

Fig. 18 Moreton event of 14 October 1999 at 09:02 UT. Images, in Hα centre and red wing, were taken with 60 s time step. (a) Hα centre. (b) Hα centre, minus the reference frame at 09:00 UT (event starting time). (c) Hα red wing, minus the reference. F, R, B indicate respectively the flare location, red and blue shifts of the propagating front (propagation direction = green arrow).

method at the 8 m spectrograph of the Pic du Midi Turret Dome. We have numerically at the inflexion points $\frac{V}{I} \approx 2.2 \times 10^{-4}$ BLOS, where BLOS is expressed in Gauss. As the slope of NaD1 wings is steep, Stokes V profiles are sharp. We observed polarization rates up to 0.20 (BLOS 1000 G) in some sunspots. In order to estimate the measurement capabilities in imagery, we have integrated the line profiles over the wavelength transmission of the NaD1 filter. The $\frac{V}{I}$ signal becomes much smaller, because the filter FWHM (W_1) is much larger than the half width (W_2) of the line derivative $\frac{dI}{d\lambda}$, which concentrates the polarimetric signal in a very narrow wave-band (Figure 19). Hence, the corrective factor to apply to the polarization rate is roughly equal to the $\frac{W_1}{W_2}$ ratio and plotted in Figure 20 for various CWL and W_1 values. Despite of the signal loss due to wavelength integration, it is of interest to consider polarimetric measurements in imagery. For that purpose, a NaD1 telescope will be tested at Meudon in the coming year in the context of a possible extension for MTSP. As the polarization rate to measure with the filter has the same order of magnitude than the photon noise of a single exposure (1% or 400 G), it is necessary to acquire many frames in order to select best images and reduce the noise, as done by Roudier et al. (2006). For example, 100 couples (I+V, I-V) will decrease the noise to 40 G. 20 G should be achieved with either 2×2 binning or with 400 couples. It must be noticed that a fast observing cadence is not required for LOS magnetograms, because the magnetic field evolves on longer time scales. The method is also, in principle, valid for the Hα telescopes, but in practice, Hα is a broad line and the sensitivity to the magnetic field is reduced by the factor 6 in comparison to NaD1.

7 Conclusion

The MTSP project is dedicated to the survey of fast evolving events in the chromosphere at the source of solar activity, such as flares and coronal mass ejections. Large flares often occur after the solar maximum (2025 for the present cycle) during a few years. MTSP, with an outstanding cadence of 10-15 s, has also the major goal to investigate Moreton waves, which are extremely fast and rare phenomena associated with largest flares. Such events are difficult to detect in the chromosphere, so that only a few cases have been studied. With systematic, fast and multi-channel observations (two Hα and one CaII K telescopes), MTSP will increase the chances to catch such phenomena. Data could be combined to SDO/AIA observations of the low corona at slower cadence (45 s) in several EUV channels. MTSP will operate automatically at Calern observatory (1270 m) under good seeing and climatic conditions. High cadence observations will be freely delivered, without any delay, to the international community through a dedicated database located at Nice computer centre. MTSP will cover cycle 25, from 2023 to, at least, the end of the present decade, where new generation solar synoptic networks could start, such as the Next Generation GONG project (Hill et al., 2019) or the Solar Physics Research Integrated Network Group (SPRING, Gosain et al. (2018)). MSTP will support Solar Orbiter (ESA) and Parker Solar Probe (NASA) operations in the coming years.

Fig. 19 Simulation of polarization measurement with the 0.36 Å FWHM NaD1 filter. Left: spectra of I+V and I-V got at Pic du Midi in an active region (wavelength in abscissa, direction of the slit in ordinates, spectral pixel 16.8 mÅ). Middle: the polarization rate $\frac{V}{I}$ with the quantity $\frac{1}{I}\frac{dI}{d\lambda}$ in the quiet Sun (yellow) and the wavelength transmittance of the filter, centred on the blue wing (green, dashed). Right: the polarization rate $\frac{V}{I}$ along the slit in the blue wing measured with the spectrograph (solid line) or extrapolated for the filter (dotted line); the dashed line is a magnification of the dotted line (ratio given by Figure 20) to recover roughly the spectroscopic signal.

Fig. 20 Simulation of the correction factor to apply to the measurements of the polarization rate with a Lorentzian filter, as a function of the FWHM (Å), for various CWL shifts (solid, dashed, dotted lines for respectively -0.12, -0.20, -0.30 Å CWL shifts). The blue inflexion point of the line is located at -0.12 Å. The red (dashed) line indicates our filter FWHM; the best CWL shift is -0.20 Å.

8 Disclosure of potential conflicts of interest

The authors declare that they have no conflicts of interest.

9 Data availability statement

The authors declare that the datasets analysed during the current study are publicly available from the corresponding author upon request.

Acknowledgements We thank the anonymous referee for useful suggestions and comments. We are indebted to Y. Bresson, C. Renaud (OCA), J.-M. Rees, C. Blanchard (OP) and the technical teams of OP and OCA for their assistance. We are also grateful for financial support to Paris and Nice observatories, the Direction Générale de l'Armement, the IDEX Plas@Par, the Programme National Soleil Terre (PNST/INSU/CNRS), the DIM ACAV (Ile de France Region) and the IDEX UCA/JEDI.

References

Admiranto AG, Priyatikanto R, Yus'an U, Puspitaningrum E (2015) Moreton waves and EIT waves related to the flare events of June 3, 2012 and July 6, 2012. In: The 5th International Conference on Mathematics and Natural Sciences, American Institute of Physics Conference Series, vol 1677, p 050014, DOI 10.1063/1.4930675, 1502.04039

Asai A, Ishii TT, Isobe H, Kitai R, Ichimoto K, UeNo S, Nagata S, Morita S, Nishida K, Shiota D, Oi A, Akioka M, Shibata K (2012) First Simultaneous Observation of an Hα Moreton Wave, EUV Wave, and Filament/Prominence Oscillations. Astrophys. J. Lett. 745(2):L18, DOI 10.1088/2041-8205/745/2/L18, 1112.5915

Balasubramaniam KS, Pevtsov AA, Neidig DF (2007) Are Moreton Waves Coronal Phenomena? Astrophys. J. 658(2):1372–1379, DOI 10.1086/512001

Cabezas DP, Asai A, Ichimoto K, Sakaue T, UeNo S, Ishitsuka JK, Shibata K (2019) Dynamic Processes of the Moreton Wave on 2014 March 29. Astrophys. J. 883(1):32, DOI 10.3847/1538-4357/ab3a39, 1908.03534

Chen PF (2011) Coronal Mass Ejections: Models and Their Observational Basis. Living Reviews in Solar Physics 8(1):1, DOI 10.12942/lrsp-2011-1

Gosain S, Roth M, Hill F, Pevtsov A, Martinez Pillet V, Thompson MJ (2018) Design of a next generation synoptic solar observing network: solar physics research integrated network group (SPRING). In: Evans CJ, Simard L, Takami H (eds) Ground-based and Airborne Instrumentation for Astronomy VII, Society of Photo-Optical Instrumentation Engineers (SPIE) Conference Series, vol 10702, p 107024H, DOI 10.1117/12.2306555

Grenat H, Laborde G (1954) Héliographe Monochromatique de Lyot. Annales d'Astrophysique 17:541

Harvey JW, Bolding J, Clark R, Hauth D, Hill F, Kroll R, Luis G, Mills N, Purdy T, Henney C, Holland D, Winter J (2011) Full-disk Solar H-alpha Images From GONG. In: AAS/Solar Physics Division Abstracts #42, AAS/Solar Physics Division Meeting, vol 42, p 17.45

Hill F, Hammel H, Martinez-Pillet V, de Wijn A, Gosain S, Burkepile J, Henney CJ, McAteer J, Bain HM, Manchester W, Lin H, Roth M, Ichimoto K, Suematsu Y (2019) ngGONG: The Next Generation GONG - A New Solar Synoptic Observational Network. In: Bulletin of the American Astronomical Society, vol 51, p 74

Krause G, Cécere M, Francile C, Costa A, Elaskar S, Schneiter M (2015) Two step mechanism for Moreton wave excitations in a blast-wave scenario: the 2006 December 06 case study. Mon. Not. Roy. Astron. Soc 453(3):2799–2807, DOI 10.1093/mnras/stv1827, 1505.02723

Krause G, Cécere M, Zurbriggen E, Costa A, Francile C, Elaskar S (2018) Are CMEs capable of producing Moreton waves? A case study: the 2006 December 6 event. Mon. Not. Roy. Astron. Soc 474(1):770–778, DOI 10.1093/mnras/stx2817

Lyot B (1944) Le Filtre Monochromatique Polarisant et ses Applications en Physique Solaire. Annales d'Astrophysique 7:31

Malherbe JM, Dalmasse K (2019) The New 2018 Version of the Meudon Spectroheliograph. Solar Phys 294(5):52, DOI 10.1007/s11207-019-1441-7

Malherbe JM, Roudier T, Moity J, Mein P, Arnaud J, Muller R (2007) Spectro polarimetry with liquid crystals. Mem. Societa Astronomica Italiana 78:203

Malherbe JM, Corbard T, Dalmasse K, Meteospace Team (2019) Meteospace, a New Instrument for Solar Survey at the Calern Observatory. Solar Phys 294(12):177, DOI 10.1007/s11207-019-1569-5

Michard R (1965) Nouvel héliographe à l'Observatoire de Meudon. L'Astronomie 79:131

Moreton GE (1960) Hα Observations of Flare-Initiated Disturbances with Velocities ~1000 km/sec. Astron. J 65:494, DOI 10.1086/108346

Narukage N, Eto S, Kadota M, Kitai R, Kurokawa H, Shibata K (2004) Moreton waves observed at Hida Observatory. In: Stepanov AV, Benevolenskaya EE, Kosovichev AG (eds) Multi-Wavelength Investigations of Solar Activity, vol 223, pp 367–370, DOI 10.1017/S1743921304006143

Oloketuyi J, Liu Y, Zhao M (2019) The Periodic and Temporal Behaviors of Solar X-Ray Flares in Solar Cycles 23 and 24. Astrophys. J 874(1):20, DOI 10.3847/1538-4357/ab064c

Pulkkinen T (2007) Space Weather: Terrestrial Perspective. Living Reviews in Solar Physics 4(1):1, DOI 10.12942/lrsp-2007-1

Reale F (2010) Coronal Loops: Observations and Modeling of Confined Plasma. Living Reviews in Solar Physics 7(1):5, DOI 10.12942/lrsp-2010-5, 1010.5927

Roudier T, Malherbe JM, Moity J, Rondi S, Mein P, Coutard C (2006) Sub arcsec evolution of solar magnetic fields. Astron. Astrophys 455(3):1091–1098, DOI 10.1051/0004-6361:20064963

Schwenn R (2006) Space Weather: The Solar Perspective. Living Reviews in Solar Physics 3(1):2, DOI 10.12942/lrsp-2006-2

Steinegger M, Hanslmeier A, Otruba W, Freislich H, Denker C, Goode PR, Marquette WM, Varied J, Wang H, Luo G, Chen D, Zhang Q (2000) An Overview of the New Global High-Resolution H-alpha Network. Hvar Observatory Bulletin 24(1):179

Stenflo J (1994) Solar Magnetic Fields: Polarized Radiation Diagnostics, vol 189. DOI 10.1007/978-94-015-8246-9

Temmer M (2021) Space weather: the solar perspective. Living Reviews in Solar

Physics 18(1):4, DOI 10.1007/s41116-021-00030-3, 2104.04261

Ueno S, Shibata K, Ichimoto K, Kitai R, Nagata S, Kimura G, Nakatani Y (2010) Continuous H-alpha Imaging Network Project (CHAIN) with Ground- based Solar Telescopes for Space Weather Research. African Skies 14:17

Warmuth A (2015) Large-scale Globally Propagating Coronal Waves. Living Reviews in Solar Physics 12(1):3, DOI 10.1007/lrsp-2015-3

Zhang H (2001) Moreton wave and its source of disturbances in the X12/3B WLF of AR6659 in 1991 June 4. *Astron. Astrophys.*372:676–685, DOI 10.1051/0004-6361:20010379

Zhang Y, Kitai R, Narukage N, Matsumoto T, Ueno S, Shibata K, Wang J (2011) Propagation of Moreton Waves. *Pub. Astron. Soc. Japan*63:685, DOI 10.1093/pasj/63.3.685